PAPER

Check for updates

A highly stable and sensitive ethanol sensor based on Ru-decorated 1D WO₃ nanowires†

Jianjun Li,[a] Qiongling Ding,[a] Xichao Mo,[a] Zihao Zou,[b] Pu Cheng,[b] Yiding Li,[b] Kai Sun,[b] Yujun Fu,[b] Yanrong Wang [ID] *[a] and Deyan He[b]

Decorating materials with noble metal catalysts is an effective method for optimizing the sensing performance of sensors based on tungsten trioxide (WO₃) nanowires. Ruthenium (Ru) exhibits excellent catalytic activity for oxygen adsorption/desorption and chemical reactions between gases and adsorbed oxygen. Herein, small Ru nanoparticles were uniformly distributed on the surface of one-dimensional WO₃ nanowires. The nanowires were prepared by the electrospinning method through an ultraviolet (UV) irradiation process, and decoration with Ru did not change their morphology. A sensor based on 4% Ru nanowires (NWs) shows the highest response (∼120) to 100 ppm ethanol, which was increased around 47 times, and the lowest ethanol detection limit (221 ppb) at a lower temperature (200 °C) displays outstanding repeatability and stability even after 45 days or in higher-humidity conditions. Moreover, it also has faster response–recovery features. The improvement in the sensing performance was attributed to the stable morphology of the nanowires, the sensitization effect of Ru, the catalytic effect of RuO₂ and the optimal atomic utilization efficiency. This work offers an effective and promising strategy for promoting the ethanol sensing performance of WO₃.

1 Introduction

The electrical properties of metal oxide semiconductors (MOS) are related to the ambient atmosphere, and they have the features of low cost, robustness, and easy synthesis.[1–3] Thus, they play a significant role in gas sensing applications to detect toxic, inflammable and explosive gases,[4–6] and are more favored by scientific researchers compared to sensors based on meta-materials[7–10] or nanophotonics.[11–13] MOS-based sensors have been reported over the past several decades, including sensors based on CuO,[14] SnO₂,[15] In₂O₃,[16] Co₃O₄,[17] Fe₂O₃,[18] ZnO,[19] and NiO,[20] for applications such as monitoring air quality and ensuring industrial safety. The discharge and leakage of volatile organic compounds (VOCs) into the environment are inevitable because of the limitations of current production technology. There is significant harm to human health when people live in an environment with VOC gases.[21–23] Thus, it is of great concern to design devices, such as sensors based on complementary infrared ray metamaterials, for the purpose of detecting VOCs.[24] Ethanol is a typical flammable and volatile colorless transparent liquid at normal temperature and pressure, and is widely used in national defense, the chemical industry, medicine and

healthcare, the food industry, and industrial and agricultural production.[25,26] In particular, ethanol vapor can form an explosive mixture with air, and it is also an inhibitor of the central nervous system.[27] Therefore, from a human health perspective, many efforts to improve the properties of sensors for monitoring ethanol are urgently needed.

Tungsten trioxide (WO₃), with a morphology that is easily controlled through various synthesis methods, is an n-type MOS material[28] and displays good gas sensitivity in the detection of NO₂,[29] xylene,[30] methanol,[31] and acetone.[32] Based on the typical gas sensing mechanism of MOS materials,[33] various methods for optimizing the sensing performance of WO₃-based sensors have been studied. These include different methods such as morphology control,[34] heterostructure construction,[35] defect introduction,[36] and metal doping or decoration. Among these methods, using noble metals (Au,[37] Pd,[38] Pt[39]) to decorate the MOS material surface is considered to be a promising strategy to boost its sensing performance due to their catalytic properties, sensitization effect, or spillover effect. However, the long-term stability of sensors prepared through the functional modification of the surface of WO₃ is usually poor. Generally, a sensing material should provide sufficient reaction sites between the target gas and adsorbed oxygen, meaning that the materials need a large specific surface area; therefore, nanomaterials are regarded as good candidate materials for fabricating sensors.

Electrospinning has become one of the main ways to effectively prepare nanomaterials due to the simple and controllable

[a] School of Physical Science and Technology, Lanzhou University, Lanzhou 730000, China. E-mail: wyr@lzu.edu.cn

[b] School of Materials and Energy, Lanzhou University, Lanzhou 730000, China

† Electronic supplementary information (ESI) available. See DOI: 10.1039/d1ra06623d

Fig. 1 (a) Schematic illustration showing preparation of WO$_3$ NWs by electrospinning, (b) the ceramic tube device, (c) schematic illustration of the experimental setup, and (d) cross-sectional view SEM image of the sensor device.

dispersion. The response value S is defined as $S = R_a/R_g$. Furthermore, the response and recovery times (τ_{res} and τ_{rec}) are defined as the time required for the value of the resistance to change by 90%.

2.4 Characterization

The structures, morphologies, and elemental compositions of the samples were characterized using field-emission scanning electron microscopy (FE-SEM, FEI Apreo-S), transmission electron microscopy (TEM, FEI Tecnai F30, operated at 300 kV), and energy-dispersive X-ray spectroscopy (EDS). X-ray powder diffraction (XRD, Malvern Panalytical) with Cu-Kα radiation (λ = 1.5406 Å) at 40 kV and 40 mA, as well as micro-Raman spectroscopy (Renishaw inVia-Reflex with an excitation wavelength of 785 nm) was used to analyze the crystalline phase

structure and composition of the samples. The surface elemental chemical states of the samples were analyzed using X-ray photoelectron spectroscopy (XPS, Kratos Axis Ultra DLD with Al Kα probe beam). The C 1s peak (284.6 eV) was used as a reference for element binding energy calibration.

3 Results and discussion

3.1 Structural and morphological characteristics

The XRD patterns of the pure and Ru-decorated WO$_3$ NWs sample are shown in Fig. 2a, demonstrating the good crystallinity of all the samples, which were well-indexed to the monoclinic structure of WO$_3$ (JCPDS card no. 72-0677). The main peaks located at $2\theta = 23.11°$, $23.58°$, and $24.35°$ correspond to the (0 0 2), (0 2 0) and (2 0 0) lattice planes of WO$_3$,
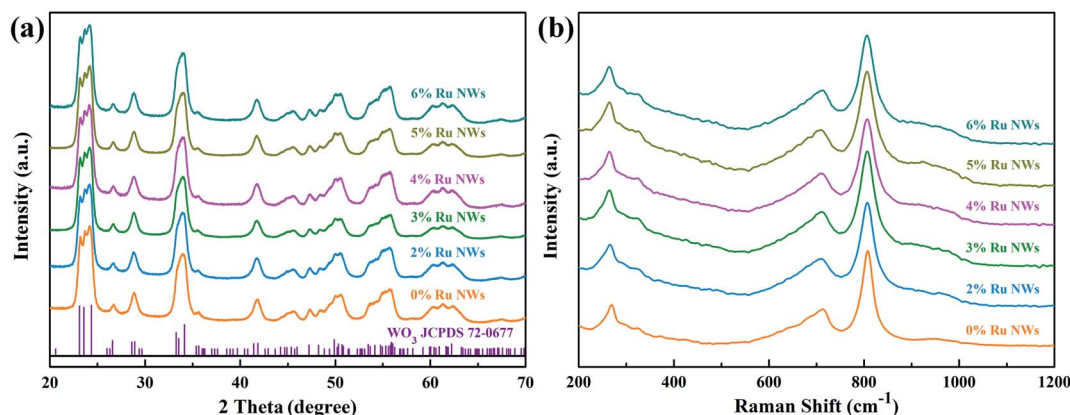
Fig. 2 (a) XRD patterns and (b) Raman spectra of 0%, 2%, 3%, 4%, 5%, and 6% Ru NWs.

© 2021 The Author(s). Published by the Royal Society of Chemistry

respectively.[52] No additional diffraction peaks corresponding to trace ruthenium or impurity phases were detected. The Raman spectra of the as-prepared samples are presented in Fig. 2b to further confirm their molecular structure information, and they illustrate that all the samples have similar spectra. The intense Raman peaks at shifts of 271 cm^{-1}, 328 cm^{-1} and 715 cm^{-1}, and 807 cm^{-1} can be assigned to the O–W–O bending vibration and stretching vibration modes of monoclinic-phase WO$_3$,[50] respectively. Overall, the XRD and Raman characterizations illustrate that the modification of the WO$_3$ NWs with a trace amount of noble metals does not affect their crystal phase or molecular structure.

The microstructures of as-prepared pure and Ru-loaded WO$_3$ NW samples were observed through SEM and TEM images. Fig. 3a–f show that the rough and porous nanowires have a uniform diameter of about 100 nm, are constructed from a large number of WO$_3$ nanoparticles, and exhibit a net structure of nanowires leading to a large mesoporous structure. This structure is beneficial for gas diffusion processes and achieving a highly sensitive response, because it has a high number of gas reaction and adsorption sites and is conducive to the diffusion or overflow of the surface of the materials.[53] A comparison of the SEM images of the different samples shows that there is no difference in their morphology. The ruthenium loading level is very low, beyond the resolution limitation of SEM, but the images indicate that the presence of Ru does not affect the microstructure of the nanowires, in line with the XRD and Raman results. Furthermore, the TEM images shown in Fig. 4a and b also show that the 0% Ru NWs and 4% Ru NWs have

a diameter of about 100 nm and are formed of many small WO$_3$ nanoparticles even after Ru decoration. Fortunately, comparison of the TEM image of the 4% Ru NWs in Fig. 4b with the image obtained from the 0% Ru NWs shows that there are abundant Ru nanoparticles with a size of several nanometers loaded on the surface of the WO$_3$ nanoparticles.

The high-resolution transmission electron microscope (HRTEM) images of the samples shown in Fig. 4c and d present the lattice information, with interplanar distances of 0.335 nm, 0.356 nm, 0.39 nm, and 0.256 nm, which can be ascribed to the (1 2 0), (2 0 0), and (0 0 1) planes of monoclinic phase WO$_3$ and the (1 0 1) planes of RuO$_2$, respectively.[21,51] The STEM image and corresponding EDS elemental mapping shown in Fig. 4e–h prove that W, O, and Ru are uniformly distributed in the 4% Ru NW sample. These results indicate that Ru is successfully decorated on the WO$_3$ NWs and mainly exists in the form of RuO$_2$.

3.2 Gas sensing performance

Determining the working temperature of sensor devices is very important for their practical application. In particular, achieving a low working temperature for sensors based on MOS is important to reduce power consumption and the risk of combustion or explosion when monitoring ethanol gas. Therefore, the relationship between the response of the sensor devices to 100 ppm ethanol over an operating temperature range of 110–230 °C was investigated, as shown in Fig. 5a. Clearly, the response values of the devices based on samples decorated with Ru increase as the working temperature
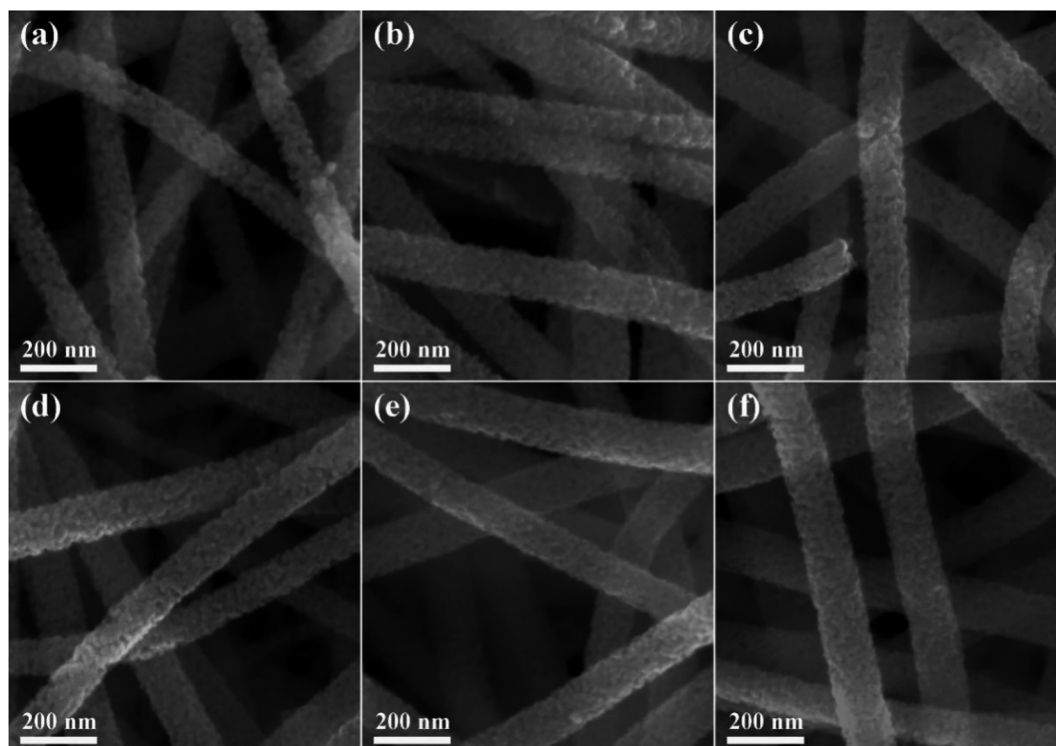
Fig. 3 SEM images of different samples: (a) 0% Ru NWs; (b) 2% Ru NWs; (c) 3% Ru NWs; (d) 4% Ru NWs; (e) 5% Ru NWs; (f) 6% Ru NWs.
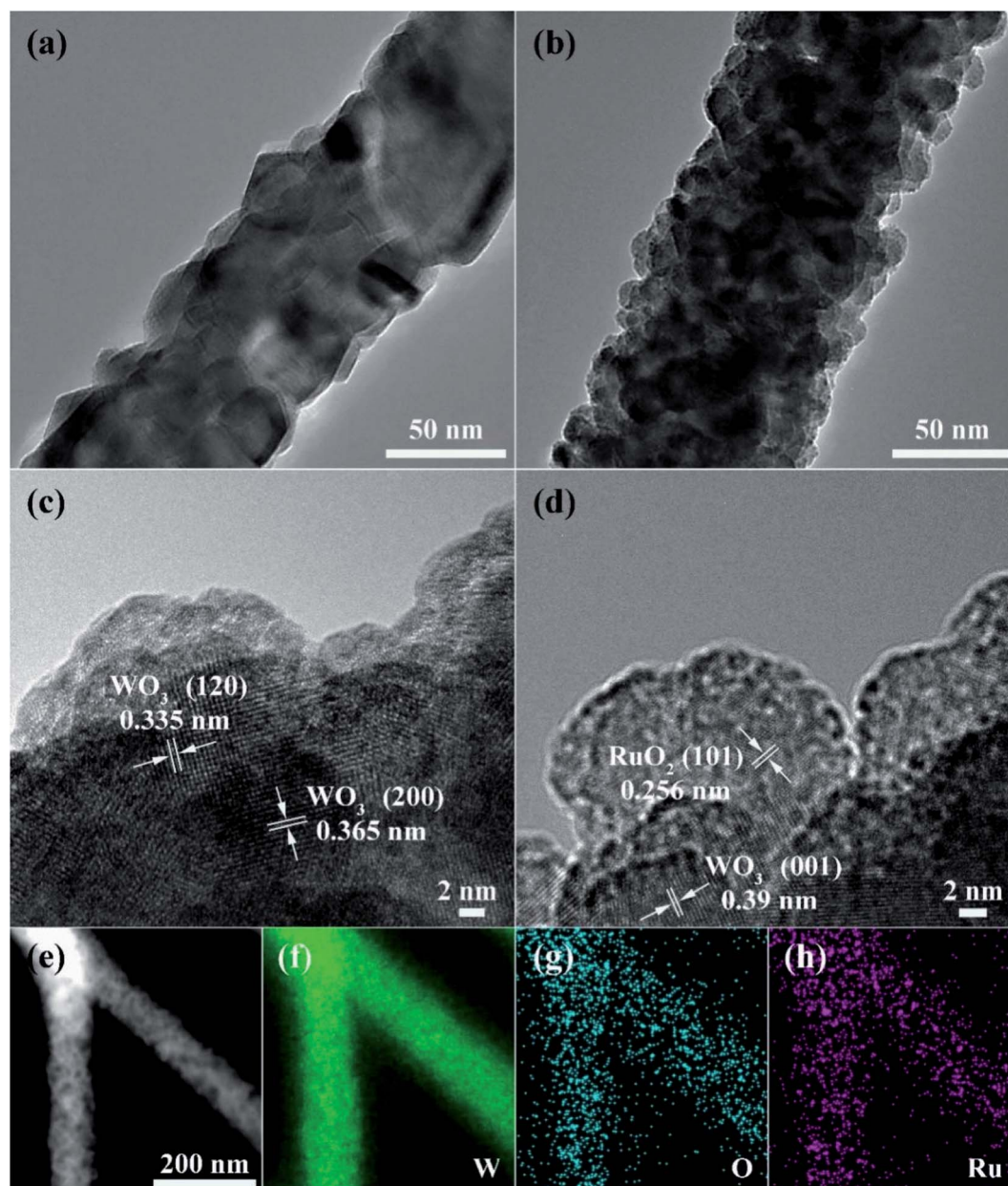
Fig. 4 TEM images of the (a) 0% Ru NWs and (b) 4% Ru NWs; (c and d) HRTEM images of the 4% Ru NWs; (e) STEM image and (f–h) corresponding element mapping images for the elements W, O, and Ru for the 4% Ru NWs.

increases in the range of 110–200 °C and decrease as the temperature increases further above 200 °C. Additionally, the response of the device based on the 0% Ru NW sample increases with temperature across the entire temperature range (as shown in the Fig. 5a inset), indicating that the optimum operating temperature of WO_3 can be reduced by introducing catalytic Ru.[51] The sensor based on 4% Ru NWs possesses the highest response to 100 ppm ethanol (120) at 200 °C, which is about 47 times higher than that of the sensor based on 0% Ru NWs under the same condition. This illustrates that decoration with Ru is a feasible method for enhancing the sensing performance of sensors based on WO_3 NWs towards ethanol.

Fig. 5b shows the dynamic response–recovery curves of the sensors towards 100 ppm ethanol at 200 °C. It is obvious that all the sensors based on Ru-decorated samples have an excellent response and recovery performance. Fig. S1a–j† displays the real-time curves of the variation of the sensor resistance at different temperatures in response to 100 ppm ethanol gas, which exhibit a classic n-type gas response phenomenon for n-type WO_3 in the detection of reducing gases. The resistance of the devices changes more rapidly due to quicker adsorption and desorption of ethanol at high temperatures compared to low temperatures. Furthermore, the resistance can be restored to its original level at any temperature. The τ_{res} and τ_{rec} of the sensors based on 0% Ru NWs towards 100 ppm ethanol at 200 °C
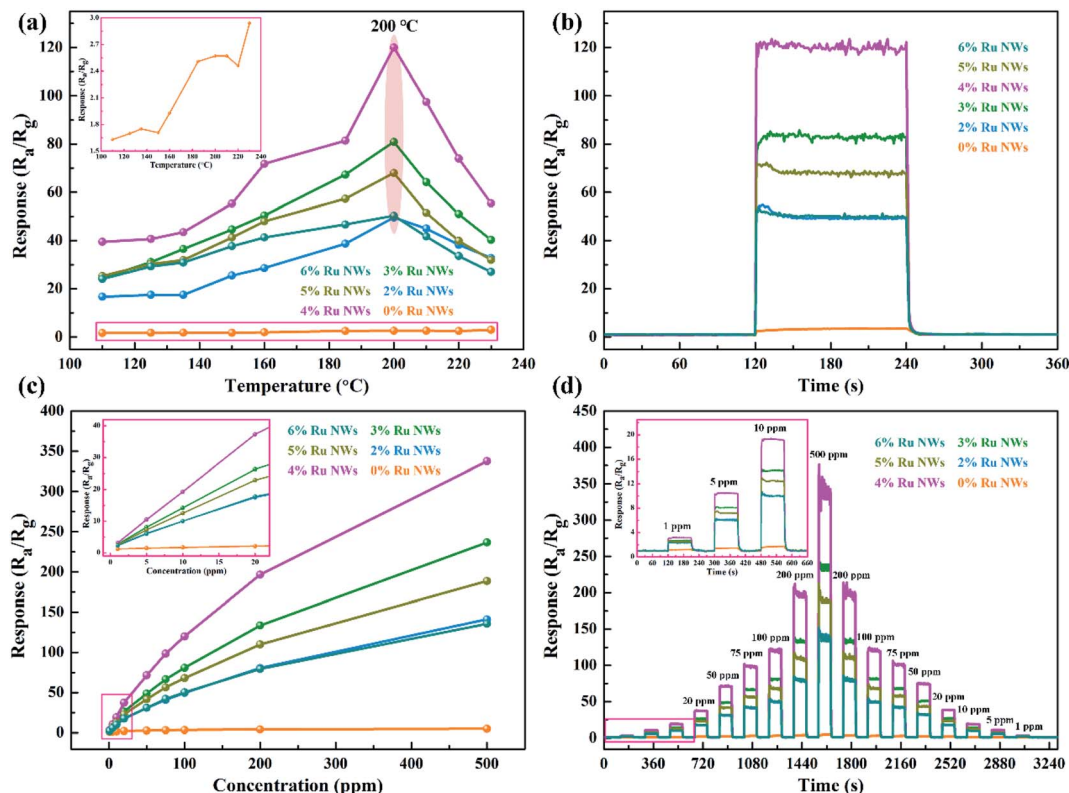
Fig. 5 (a) The responses of the samples towards 100 ppm ethanol as a function of operating temperature; the inset corresponds to the device based on 0% Ru NWs. (b) The dynamic response–recovery curves of the samples towards 100 ppm ethanol at 200 °C. (c) Curves of the responses toward various concentrations (1, 5, 10, 20, 50, 75, 100, 200, and 500 ppm) of ethanol gas for the samples. (d) The dynamic response–recovery curves of the sensors towards concentrations of ethanol of up to 500 ppm followed by down to 1 ppm; the inset corresponds to a low concentration (1–20 ppm) at 200 °C.

obtained from Fig. S1k and l† are 23 s and 58 s, and the corresponding values for the sensor based on 4% Ru NWs are 1 s and 18 s, respectively. This enhanced performance is ascribed to the catalytic effect of Ru, which promotes the chemical reaction between the target gas and adsorbed oxygen as well as the desorption of ethanol.[54] Fig. S2† shows the baseline resistance of sensors at various temperatures under air; it can be found that the resistance value decreases with increasing temperature, which is a typical characteristic of semiconductor materials. The resistance values of the sensors based on Ru-

decorated WO₃ NWs are larger than those of the sensor based on the pure WO₃ NWs, which is ascribed to the widening of the depletion layer caused by the transition of electrons from the MOS to the noble metal. The sensing performance of the sensors in this work is compared to that of previously reported materials based on WO₃ in Table 1. These Ru-decorated WO₃ NWs evidently display outstanding sensing performance towards ethanol, with the best response among the compared materials and a lower optimum working temperature.

Table 1 Comparison of previous works and this work in terms of ethanol gas sensing performance[a]

Sample	T_{op} (°C)	Conc. (ppm)	Response (S)	Ref.
Core–shell WO₃–SnO₂ nanofibers	280	10	5.09	55
WO₃–SnO₂ composite coating	250	300	1.73	56
Ce-doped WO₃	350	1	12.3	57
WO₃·H₂O network	350	100	16	25
Ga₂O₃–WO₃ heterostructures	275	100	14	58
Au-decorated WO₃	200	100	57	59
ZnO–WO₃ composite nanorods	300	50	16.2	60
Ru-decorated WO₃	200	100	78	This work

[a] T_{op}: optimum working temperature of the sensors.
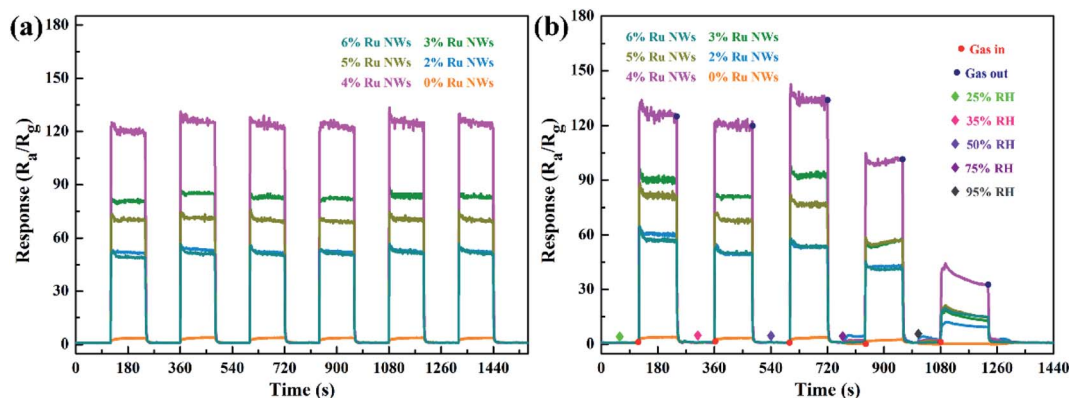
Fig. 6 (a) Repeatability test of the dynamic response curves of the sensors over six cycles, and (b) the dynamic response curves of the sensors under different RH (%) towards 100 ppm ethanol at 200 °C.

The response values of all the devices as a function of ethanol concentration (from 1 to 500 ppm) at their optimal working temperature are shown in Fig. 5c. As can be seen, the response values of the sensors increase with increasing ethanol concentration, and the worst sensing performance is achieved using the sensors based on the 0% Ru NW sample. In contrast, the 4%-Ru-NW-based sensor displays an outstanding response. Additionally, the response of the sensor based on 0% Ru NWs only increases slightly when the concentration of ethanol gas is increased, while the responses of the sensors based on Ru-decorated NWs increase rapidly. Importantly, the response value increases almost linearly at low ethanol concentrations (1–20 ppm), and there is no saturation trend as the ethanol concentration increases to 500 ppm. Furthermore, the dynamic response and recovery curves and corresponding ethanol response as a function of concentration for every sensor are shown in Fig. 5d and S3a,† and demonstrate good symmetry when the ethanol concentration is increased and then decreased. Additionally, Fig. S3b† shows the relationship between $\ln(S)$ and $\ln(C)$ at the optimum sensor working temperature. The experimental data can be fitted well by a linear function, and show that the ethanol detection limit was 759 ppb, 290 ppb, 257 ppb, 211 ppb, 270 ppb and 303 ppb, respectively, for the sensor devices based on the 0%, 2%, 3%, 4%, 5%, and 6% Ru NW materials.

When a varying amount of ethanol gas is injected, the response is immediate and quickly achieves stability. The resistance returns to its previous level when the devices are exposed to air, even for an ethanol concentration of 1 ppm. Fig. 6a shows six response cycles towards 100 ppm ethanol at 200 °C. There is a slight increase in the response, which is ascribed to the surfaces of the materials being activated by ethanol. The result illustrates the outstanding repeatability and reproducibility of these sensors. Overall, these results prove that the sensors have the potential to sensitively detect ethanol across a wide range of practical conditions.

Moisture negatively affects gas sensors,[18] so the effect of increasing humidity was investigated in this work. Fig. 6b displays the dynamic response curves of sensors exposed to
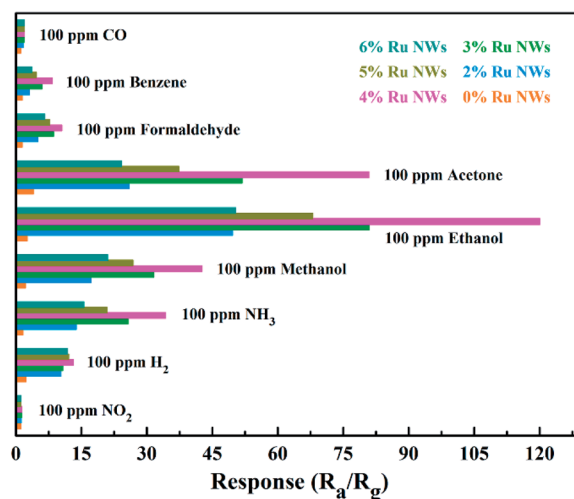
Fig. 7 Selectivity patterns of the sensors towards various gases (100 ppm benzene, formaldehyde, acetone, methanol, NH_3, CO, NO_2, H_2, and ethanol) at 200 °C.

ethanol under different RH conditions (25%, 35%, 50%, 75%, and 95%). There is only a slight change in the gas response even at 75% RH, although the sensors show better performance when the RH is 50%. The resistance of the devices slowly increases in a stable manner when the sensors are tested in a 95% RH environment. This is because water molecules occupy the gas and oxygen reaction sites, inhibiting the response. Such humidity effects are acceptable for practical application.

Selectivity is also a crucial factor for the practical application of sensor devices. The response of all the sensors exposed to 100 ppm of the gases CO, NH_3, benzene, acetone, methanol, formaldehyde, NO_2, and H_2 were analyzed and are displayed in Fig. 7. The Ru-decorated sensors clearly demonstrate better sensing performance of all the VOC gases compared to the 0% Ru NWs sensor. Compared with their response to other gases, the sensors display optimal performance for the detection of ethanol. The sensor offers decent selectivity between ethanol
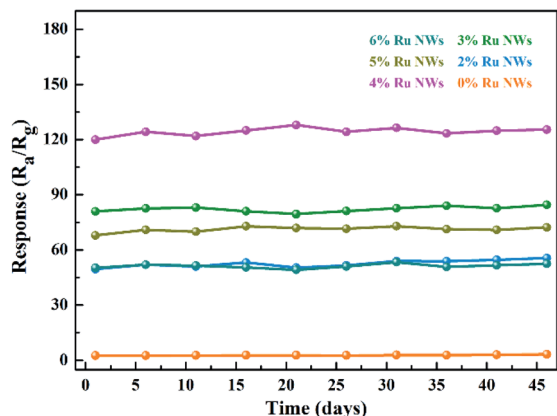
Fig. 8 Long-term stability of sensors towards 100 ppm ethanol at 200 °C.

highest response to ethanol, while their sensing performance toward other VOCs is also enhanced. The statistics of the initial resistance for the sensor selectivity and repeatability tests (Fig. S4†) illustrates that the devices can almost completely recover after exposure to the tested gases, further demonstrating the outstanding repeatability of the sensors.

Gas sensors based on MOS are always limited in practical application by poor long-term stability performance; therefore, more stable sensor materials are required. As shown in Fig. 8 and S5,† the prepared sensors based on WO_3 NWs demonstrate extremely stable performance for practical ethanol detection. The sensing performance is even slightly increased after 45 days, and the dynamic response and recovery curves have the same characteristics, as shown in Fig. 6a. In brief, these sensors have good moisture resistance, selectivity and long-term stability.

and CO, benzene, formaldehyde, and NO_2. However, the selectivity towards ethanol over acetone, methanol and ammonia is not as satisfactory. The selectivity towards acetone is unsatisfactory, which is ascribed to the fact that the samples without Ru modification showed the best sensing performance towards acetone. The introduction of Ru can effectively break C–C bonds in VOCs, and the ethoxy species of ethanol are always present as monodentates with their oxygen atom bound to one Ru atom. Thus, the sensors based on Ru-decorated materials show the

3.3 Mechanism

The resistance value of the sensors is stable in conditions where air is the background due to a dynamic equilibrium between the oxygen adsorption and desorption processes. Currently, the widely accepted sensing mechanism of typical n-type MOS (WO_3) materials for the detection of reducing gases (ethanol) is attributed to the change in carrier concentration due to the capture and release of electrons during the chemical reaction between the target gas and the oxygen species adsorbed on the MOS surface.[33,61] Therefore, the movement of electrons and the
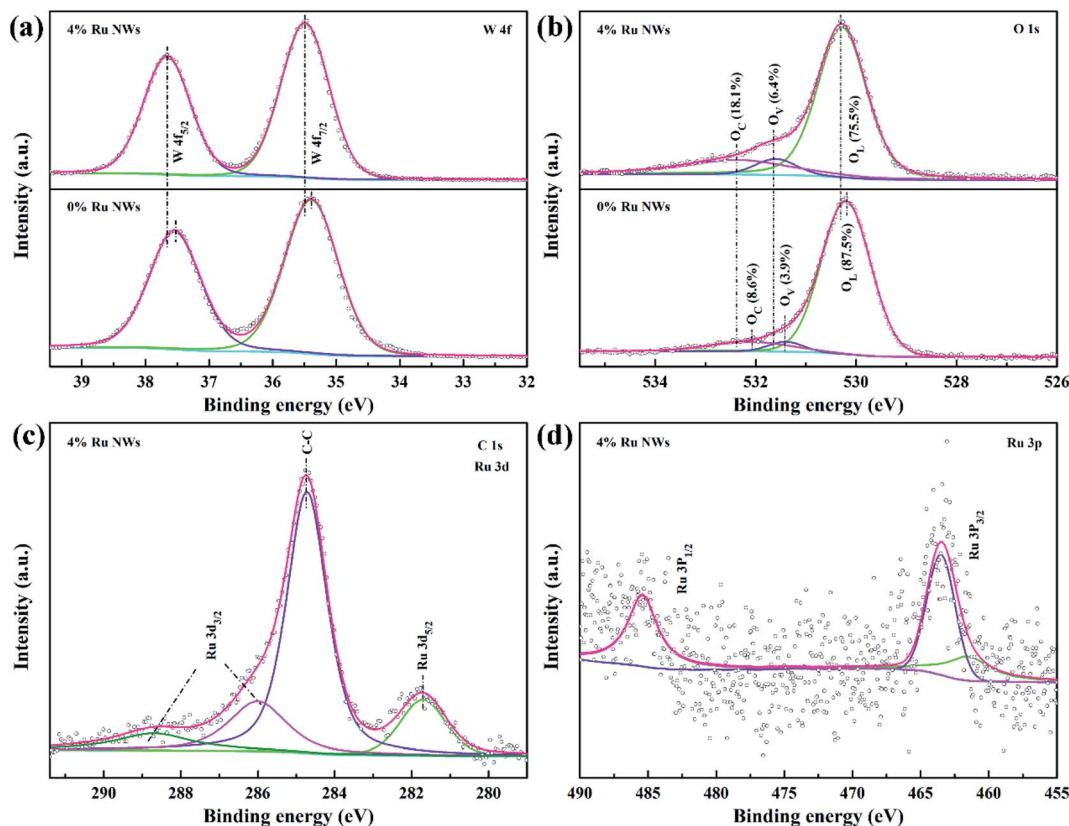
Fig. 9 (a) W 4f, (b) O 1s XPS spectra of 0% Ru NWs, and 4% Ru NWs samples, (c) Ru 3d and (d) Ru 3p spectra of 4% Ru NWs samples.
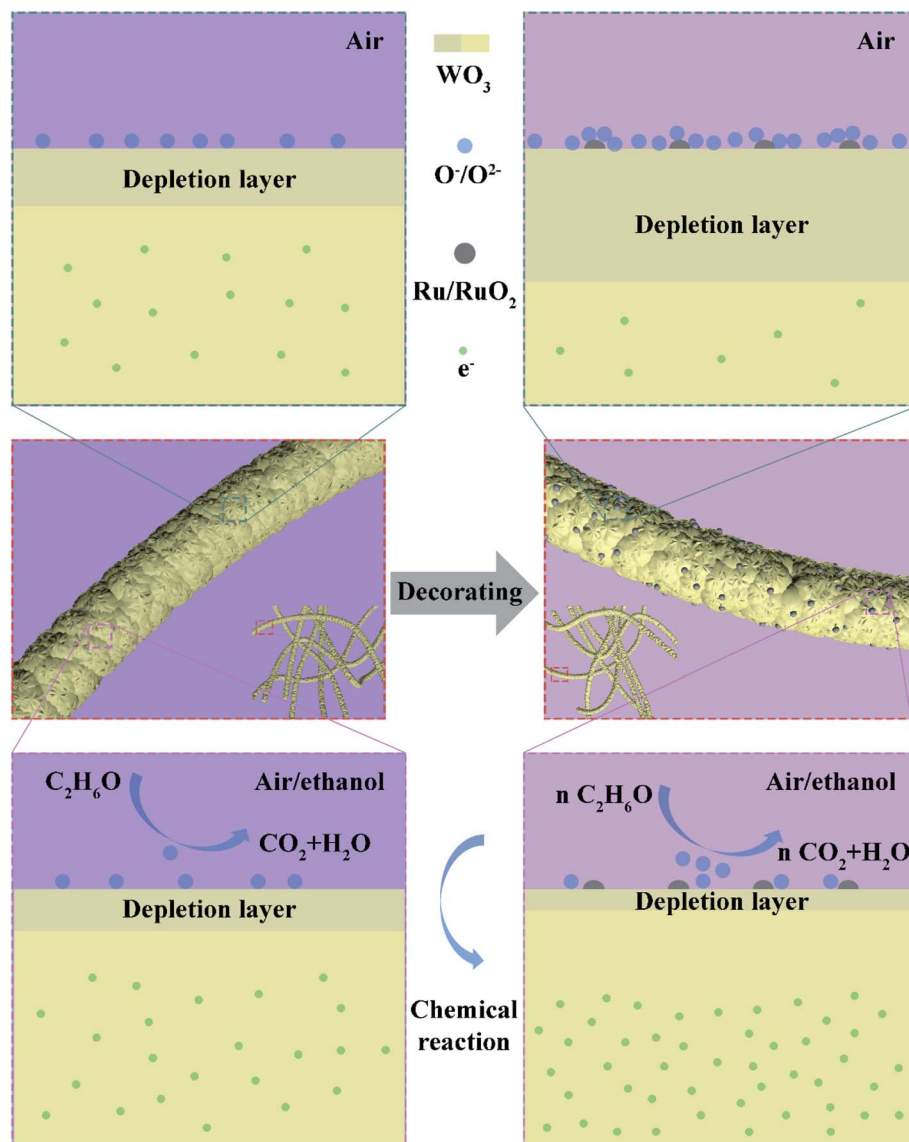
Fig. 10 Schematic diagram of pure and Ru-decorated WO_3 NWs and their ethanol sensing mechanism and its enhancement.

changes in adsorbed oxygen species on the surface of the materials when the sensors are exposed to alternating atmospheres under a certain concentration of the target gas should be investigated. The conduction band electrons can be trapped by oxygen to form chemisorbed oxygen species; this process is highly dependent on the working temperature in air ($O_{2\ (ads)} + 2e^- \leftrightarrow 2O^-_{(ads)}$ ($100\ °C < T < 300\ °C$)).[22] The trapped electrons are released back to the conduction band with the introduction of reducing gas (the gas will undergo an oxidation–reduction reaction with the adsorbed oxygen, releasing electrons to participate in conduction).[28] As a result, an electron depletion layer is formed on the surface of the sensing materials in air, and the width of this depletion layer is reduced in testing; this leads to the change in the resistance of the sensing materials, consistent with Fig. S1.†

The improvement in the sensing performance can be explained by the electronic and chemical sensitization of Ru.

The 0% Ru NW and 4% Ru NW samples were characterized using XPS (Fig. S6† and 9) to analyze the chemical states of elements (W, O, and Ru) and the sample compositions. The comparison of the full survey spectra shown in Fig. S6† clearly shows a weak peak at around 282 eV and a slight change at around 463 eV for the Ru-decorated sample, corresponding to Ru 3d and Ru 3p, respectively. The Ru 3p peak, which is only present in the 4% Ru NWs samples, illustrates the presence of Ru. The high-resolution spectra of W 4f, O 1s, Ru 3d, and Ru 3p are shown in Fig. 9a–d. Fig. 9a displays two peaks at 35.5 ± 0.1 eV (W $4f_{7/2}$) and 37.6 ± 0.1 eV (W $4f_{5/2}$), corresponding to the W^{6+} oxidation state. In the O 1s XPS spectrum in Fig. 9b, there are three major peaks located at 530.25 ± 0.1 eV, 531.5 ± 0.1 eV, and 532.2 ± 0.1 eV, which are respectively ascribed to lattice oxygen (O_L), oxygen vacancies (O_V), and chemisorbed oxygen (O_C) on the WO_3 surface.

Decorating the WO_3 NWs with 4% Ru increases the amount of O_V from 3.9% to 6.4%, providing more reaction sites for target gases, and increases O_C from 8.6% to 18.1%, indicating that more chemisorbed oxygen can participate in the chemical reaction.[36] This explains the larger response of the Ru-decorated WO_3. Additionally, as shown in Fig. 9c, the XPS peaks of Ru 3d overlap with the C 1s peak. The peaks located at 281.7 eV and around 286 eV correspond to Ru $3d_{5/2}$ and Ru $3d_{3/2}$. The Ru 3p XPS spectrum displayed in Fig. 9d illustrates that ruthenium is in the form of RuO_2.[62] Importantly, both the W 4f and O 1s peaks of the 4% Ru NWs spectrum shift to higher binding energy positions, indicating that the electron migration direction between WO_3 and Ru is from the semiconductor to the noble metal. This leads to a higher resistance state of the devices based on the Ru-decorated samples, in line with Fig. S1 and S2.† This also proves the interaction between Ru and WO_3. Their synergy is conducive to the improvement of the sensing performance. In addition, RuO_2 is a p-type MOS; therefore, a p–n heterojunction is formed at the interface between RuO_2 and WO_3. Additionally, the work function of RuO_2 is higher than that of WO_3, so electrons will migrate from WO_3 to RuO_2 until their Fermi levels are balanced.[63] This widens the electron depletion layer, which is beneficial for enhancing the sensitivity of WO_3. Because a lower electron concentration means a higher baseline resistance of the sensors in air, this results in a higher response based on the equation $S = R_a/R_g$. The ethanol sensing mechanism and enhancement for pure and Ru-decorated samples are shown in Fig. 10.

The devices based on Ru-decorated samples have a lower optimal operating temperature and faster response and recovery. This is ascribed to the catalytic effect of RuO_2, which reduces the activation energy of the gas to react with adsorbed oxygen and accelerates the dynamic equilibrium of the oxygen adsorption and desorption processes. The gas sensing property of the samples improves with increasing Ru decoration up to 4 at%. Above this, the gas sensing property deteriorates, which can be explained by the lower atom utilization efficiency under the same conditions.[64] The stability of these sensors is attributed to the nature of the WO_3 NWs. The materials were annealed at 500 °C during the preparation process, and the sensors underwent a high-temperature aging treatment, enhancing material stability.

4 Conclusions

In summary, various amounts of the noble metal Ru were used to functionalize the surface of WO_3 NWs prepared by a traditional electrospinning method *via* a facile and low-cost UV irradiation process. In particular, the sensor device based on 4% Ru-decorated WO_3 NWs achieves the most outstanding performance for ethanol detection at a low working temperature of 200 °C, with a response 47 times higher than that of undecorated WO_3 NWs. The response of the prepared sensors to step changes in the concentration of ethanol is clearly distinguished. The lowest detection limit level is 221 ppb. Furthermore, these sensors exhibit good repeatability and stability even after 45 days or under high relative humidity conditions. This

can be ascribed to the higher level of oxygen vacancies and surface chemically adsorbed oxygen species on the Ru-decorated WO_3 caused by the electronic/chemical sensitization effect of Ru, the catalytic effect of RuO_2, the optimized atomic utilization efficiency, and the heterojunction formed at the interface between WO_3 and RuO_2. Overall, this work clearly proves that using Ru to decorate the surface of a MOS is an effective and promising method for promoting ethanol sensing performance.

Author contributions

Jianjun Li: conceptualization, methodology, formal analysis, validation, data curation, writing—original draft, writing—review & editing. Qiongling Ding: methodology. Xichao Mo: data collection, investigation. Zihao Zou: data collection, investigation. Pu Cheng: data collection. Yiding Li: data collection. Kai Sun: data collection. Yujun Fu: data collection, supervision. Yanrong Wang: conceptualization, methodology, funding acquisition, writing—original draft, writing—review & editing, supervision. Deyan He: conceptualization, supervision. All authors have read and agreed to the published version of the manuscript.

Conflicts of interest

The authors declare no competing interest.

Acknowledgements

References

1 Y. Wang, P. Cheng, X. Li, C. Wang, C. Feng and G. Lu, Revealing the relationship between the Au decoration method and the enhanced acetone sensing performance of a mesoporous In_2O_3-based gas sensor, *J. Mater. Chem. C*, 2020, **8**, 78–88.

2 A. Staerz, S. Somacescu, M. Epifani, T. Kida, U. Weimar and N. Barsan, WO_3-based gas sensors: identifying inherent qualities and understanding the sensing mechanism, *ACS Sens.*, 2020, **5**, 1624–1633.

3 K. Xu, N. Liao, B. Zheng and H. Zhou, Adsorption and diffusion behaviors of H_2, H_2S, NH_3, CO and H_2O gases molecules on MoO_3 monolayer: A DFT study, *Phys. Lett. A*, 2020, **384**, 126533.

4 H. Yu, J. Li, Z. Li, Y. Tian and Z. Yang, Enhanced formaldehyde sensing performance based on Ag@WO_3 2D nanocomposite, *Powder Technol.*, 2019, **343**, 1–10.

5 Z. Zhu, C.-T. Kao and R.-J. Wu, A highly sensitive ethanol sensor based on Ag@TiO_2 nanoparticles at room temperature, *Appl. Surf. Sci.*, 2014, **320**, 348–355.

6 T. Tesfamichael, Electron beam evaporation of tungsten oxide films for gas sensors, *IEEE Sens. J.*, 2010, **10**, 1796–1802.

7 J. Yang and Y. S. Lin, Design of tunable terahertz metamaterial sensor with single- and dual-resonance characteristic, *Nanomaterials*, 2021, **11**, 2221.

8 Z. Liang, Y. Wen, Z. Zhang, Z. Liang, Z. Xu and Y.-S. Lin, Plasmonic metamaterial using metal-insulator-metal nanogratings for high-sensitive refraction index sensor, *Results Phys.*, 2019, **15**, 102602.

9 J. Zhong, X. Xu and Y. S. Lin, Tunable terahertz metamaterial with electromagnetically induced transparency characteristic for sensing application, *Nanomaterials*, 2021, **11**, 2175.

10 Y. Zhang, P. Lin and Y. S. Lin, Tunable split-disk metamaterial absorber for sensing application, *Nanomaterials*, 2021, **11**, 598.

11 Z. Lin, Z. Xu, P. Liu, Z. Liang and Y.-S. Lin, Polarization-sensitive terahertz resonator using asymmetrical F-shaped metamaterial, *Opt. Laser Technol.*, 2020, **121**, 105826.

12 Y.-S. Lin, Complementary infrared metamaterials for volatile organic solutions sensing, *Mater. Lett.*, 2017, **195**, 55–57.

13 Y. Wen, Z. Liang and Y.-S. Lin, Tunable perfect meta-absorber with high-sensitive polarization characteristic, *Advanced Photonics Research*, 2020, **2**, 2000027.

14 H. Zhang, H. Li, L. Cai, Q. Lei, J. Wang, W. Fan, *et al.*, Performances of In-doped CuO-based heterojunction gas sensor, *J. Mater. Sci.: Mater. Electron.*, 2019, **31**, 910–919.

15 Y. Wang, Z. Zhao, Y. Sun, P. Li, J. Ji, Y. Chen, *et al.*, Fabrication and gas sensing properties of Au-loaded SnO2 composite nanoparticles for highly sensitive hydrogen detection, *Sens. Actuators, B*, 2017, **240**, 664–673.

16 D. Zhang, Y. Cao, Z. Yang and J. Wu, Nanoheterostructure construction and DFT study of Ni-Doped In2O3 nanocubes/WS2 hexagon nanosheets for formaldehyde sensing at room temperature, *ACS Appl. Mater. Interfaces*, 2020, **12**, 11979–11989.

17 J. M. Xu and J. P. Cheng, The advances of Co3O4 as gas sensing materials: A review, *J. Alloys Compd.*, 2016, **686**, 753–768.

18 C. Zhang, S. Zhang, Y. Yang, H. Yu and X. Dong, Highly sensitive H2S sensors based on metal-organic framework driven γ-Fe2O3 on reduced graphene oxide composites at room temperature, *Sens. Actuators, B*, 2020, **325**, 128804.

19 Z. Wang, Z. Tian, D. Han and F. Gu, Au-modified three-dimensionally ordered macroporous ZnO:In for high-performance ethanol sensors, *J. Mater. Chem. C*, 2020, **8**, 2812–2819.

20 T. P. Mokoena, Z. P. Tshabalala, K. T. Hillie, H. C. Swart and D. E. Motaung, The blue luminescence of p-type NiO nanostructured material induced by defects: H2S gas sensing characteristics at a relatively low operating temperature, *Appl. Surf. Sci.*, 2020, **525**, 146002.

21 X. Chang, S. Xu, S. Liu, N. Wang, S. Sun, X. Zhu, *et al.*, Highly sensitive acetone sensor based on WO3 nanosheets derived from WS2 nanoparticles with inorganic fullerene-like structures, *Sens. Actuators, B*, 2021, **343**, 130135.

22 Q. Ding, Y. Wang, P. Guo, J. Li, C. Chen, T. Wang, *et al.*, Cr-doped urchin-like WO3 hollow spheres: the cooperative modulation of crystal growth and energy-band structure for high-sensitive acetone detection, *Sensors*, 2020, **20**, 3473.

23 H. Gao, Y. Ma, P. Song, Z. Yang and Q. Wang, Cu-doped Fe2O3 porous spindles derived from metal-organic frameworks with enhanced sensitivity to triethylamine, *Mater. Sci. Semicond. Process.*, 2021, **123**, 105510.

24 Y.-S. Lin and W. Chen, A large-area, wide-incident-angle, and polarization-independent plasmonic color filter for glucose sensing, *Opt. Mater.*, 2018, **75**, 739–743.

25 S. Liu, W. Zeng and Y. Li, Synthesis of spherical WO3·H2O network for ethanol sensing application, *Mater. Lett.*, 2019, **253**, 42–45.

26 D. Zhang, Y. Cao, J. Wu and X. Zhang, Tungsten trioxide nanoparticles decorated tungsten disulfide nanoheterojunction for highly sensitive ethanol gas sensing application, *Appl. Surf. Sci.*, 2020, **503**, 144063.

27 Q. Li, D. Chen, J. Miao, S. Lin, Z. Yu, D. Cui, *et al.*, Highly sensitive sensor based on ordered porous ZnO nanosheets for ethanol detecting application, *Sens. Actuators, B*, 2021, **326**, 128952.

28 C. Dong, R. Zhao, L. Yao, Y. Ran, X. Zhang and Y. Wang, A review on WO3 based gas sensors: morphology control and enhanced sensing properties, *J. Alloys Compd.*, 2020, **820**, 153194.

29 J. Qi, K. Chen, Y. Xing, H. Fan, H. Zhao, J. Yang, *et al.*, Application of 3D hierarchical monoclinic-type structural Sb-doped WO3 towards NO2 gas detection at low temperature, *Nanoscale*, 2018, **10**, 7440–7450.

30 L. Deng, X. Ding, D. Zeng, S. Zhang and C. Xie, High sensitivity and selectivity of C-doped WO3 gas sensors toward toluene and xylene, *IEEE Sens. J.*, 2012, **12**, 2209–2214.

31 Y. Zeng, Z. Hua, X. Tian, X. Li, Z. Qiu, C. Zhang, *et al.*, Selective detection of methanol by zeolite/Pd-WO3 gas sensors, *Sens. Actuators, B*, 2018, **273**, 1291–1299.

32 Z. Qiu, Z. Hua, Y. Li, M. Wang, D. Huang, C. Tian, *et al.*, Acetone sensing properties and mechanism of Rh-loaded WO3 Nanosheets, *Front. Chem.*, 2018, **6**, 385.

33 J. Dai, O. Ogbeide, N. Macadam, Q. Sun, W. Yu, Y. Li, *et al.*, Printed gas sensors, *Chem. Soc. Rev.*, 2020, **49**, 1756–1789.

34 K. T. Alali, J. Liu, K. Aljebawi, P. Liu, R. Chen, R. Li, *et al.*, Electrospun n-p WO3/CuO heterostructure nanofibers as an efficient sarin nerve agent sensing material at room temperature, *J. Alloys Compd.*, 2019, **793**, 31–41.

35 H. Shao, M. Huang, H. Fu, S. Wang, L. Wang, J. Lu, *et al.*, Hollow WO3/SnO2 hetero-nanofibers: controlled synthesis and high efficiency of acetone vapor detection, *Front. Chem.*, 2019, **7**, 785.

36 J. Lu, C. Xu, L. Cheng, N. Jia, J. Huang and C. Li, Acetone sensor based on WO3 nanocrystallines with oxygen defects for low concentration detection, *Mater. Sci. Semicond. Process.*, 2019, **101**, 214–222.

37 S. Kabcum, N. Kotchasak, D. Channei, A. Tuantranont, A. Wisitsoraat, S. Phanichphant, *et al.*, Highly sensitive

and selective NO$_2$ sensor based on Au-impregnated WO$_3$ nanorods, *Sens. Actuators, B*, 2017, **252**, 523–536.

38 A. Nikfarjam, S. Fardindoost and A. Iraji zad, Fabrication of Pd doped WO$_3$ nanofiber as hydrogen sensor, *Polymers*, 2013, **5**, 45–55.

39 C.-H. Chang, T.-C. Chou, W.-C. Chen, J.-S. Niu, K.-W. Lin, S.-Y. Cheng, *et al.*, Study of a WO$_3$ thin film based hydrogen gas sensor decorated with platinum nanoparticles, *Sens. Actuators, B*, 2020, **317**, 128145.

40 P. V. Morais, P. H. Suman, R. A. Silva and M. O. Orlandi, High gas sensor performance of WO$_3$ nanofibers prepared by electrospinning, *J. Alloys Compd.*, 2021, **864**, 158745.

41 S. J. Choi, S. Chattopadhyay, J. J. Kim, S. J. Kim, H. L. Tuller, G. C. Rutledge, *et al.*, Coaxial electrospinning of WO$_3$ nanotubes functionalized with bio-inspired Pd catalysts and their superior hydrogen sensing performance, *Nanoscale*, 2016, **8**, 9159–9166.

42 P. P. Mane, R. S. Ambekar and B. Kandasubramanian, Electrospun nanofiber-based cancer sensors: A review, *Int. J. Pharm.*, 2020, **583**, 119364.

43 G. Korotcenkov, Electrospun metal oxide nanofibers and their conductometric gas sensor application. Part 2: gas sensors and their advantages and limitations, *Nanomaterials*, 2021, **11**, 1555.

44 P. Su, W. Pei, X. Wang, Y. Ma, Q. Jiang, J. Liang, *et al.*, Exceptional electrochemical HER performance with enhanced electron transfer between Ru nanoparticles and single atoms dispersed on a carbon substrate, *Angew. Chem., Int. Ed. Engl.*, 2021, **60**, 16044–16050.

45 M. Gao, H. Tan, P. Zhu, J. Zhang, H. Wang, X. Liu, *et al.*, Why phenol is selectively hydrogenated to cyclohexanol on Ru (0001): an experimental and theoretical study, *Appl. Surf. Sci.*, 2021, **558**, 149880.

46 H. P. Pacheco, E. F. de Souza, S. M. Landi, M. V. David, J. Tyler Prillaman, R. J. Davis, *et al.*, Ru Promoted MgO and Al-Modified MgO for Ethanol Upgrading, *Top. Catal.*, 2019, **62**, 894–907.

47 A. Rodríguez-Gómez, E. Lepre, L. Sánchez-Silva, N. López-Salas and A. R. de la Osa, PtRu nanoparticles supported on noble carbons for ethanol electrooxidation, *J. Energy Chem.*, 2022, **66**, 168–180.

48 L. Wei, F. Liu, X. Jiang, Y.-H. Yang, T. Sheng, Q.-Q. Xu, *et al.*, High-index faceted Pt-Ru alloy concave nanocubes with enhancing ethanol and CO electro-oxidation, *Electrochim. Acta*, 2021, **396**, 139266.

49 A. Waheed, X. Wang, N. Maeda, S. Naito and A. Baiker, Surface processes occurring during aqueous phase ethanol reforming on Ru/TiO$_2$ tracked by ATR-IR spectroscopy, *Appl. Catal., A*, 2019, **581**, 111–115.

50 D. Huang, W. Yuan, S. Fan, C. Tian, Z. Hua, X. Tian, *et al.*, Hydrogen sensing mechanism of Ru-loaded WO$_3$ nanosheets, *Sens. Actuators, B*, 2020, **304**, 127339.

51 Y. Li, Z. Hua, Y. Wu, Y. Zeng, Z. Qiu, X. Tian, *et al.*, Modified impregnation synthesis of Ru-loaded WO$_3$ nanoparticles for acetone sensing, *Sens. Actuators, B*, 2018, **265**, 249–256.

52 H. Li, S. Chu, Q. Ma, J. Wang, Q. Che, G. Wang, *et al.*, Hierarchical WO$_3$/ZnWO$_4$ 1D fibrous heterostructures with tunable *in situ* growth of WO$_3$ nanoparticles on surface for efficient low concentration HCHO detection, *Sens. Actuators, B*, 2019, **286**, 564–574.

53 X. Kou, F. Meng, K. Chen, T. Wang, P. Sun, F. Liu, *et al.*, High-performance acetone gas sensor based on Ru-doped SnO$_2$ nanofibers, *Sens. Actuators, B*, 2020, **320**, 128292.

54 S. S. Mehta, D. Y. Nadargi, M. S. Tamboli, L. S. Chaudhary, P. S. Patil, I. S. Mulla, *et al.*, Ru-loaded mesoporous WO$_3$ microflowers for dual applications: enhanced H$_2$S sensing and sunlight-driven photocatalysis, *Dalton Trans.*, 2018, **47**, 16840–16845.

55 F. Li, X. Gao, R. Wang and T. Zhang, Design of WO$_3$-SnO$_2$ core-shell nanofibers and their enhanced gas sensing performance based on different work function, *Appl. Surf. Sci.*, 2018, **442**, 30–37.

56 V. Ambardekar, P. P. Bandyopadhyay and S. B. Majumder, Understanding on the ethanol sensing mechanism of atmospheric plasma sprayed 25 wt. % WO$_3$-75 wt. % SnO$_2$ coating, *Sens. Actuators, B*, 2019, **290**, 414–425.

57 Q. Diao, Y. Yin, W. Jia, X. Xu, Y. Ding, X. Zhang, *et al.*, Highly sensitive ethanol sensor based on Ce-doped WO$_3$ with raspberry-like architecture, *Mater. Res. Express*, 2020, **7**, 115012.

58 Z. Wei, M. K. Akbari, Z. Hai, R. K. Ramachandran, C. Detavernier, F. Verpoort, *et al.*, Ultra-thin sub-10nm Ga$_2$O$_3$-WO$_3$ heterostructures developed by atomic layer deposition for sensitive and selective C$_2$H$_5$O$_H$ detection on ppm level, *Sens. Actuators, B*, 2019, **287**, 147–156.

59 J. Ma, X. Xiao, Y. Zou, Y. Ren, X. Zhou, X. Yang, *et al.*, A general and straightforward route to noble metal-decorated mesoporous transition-metal oxides with enhanced gas sensing performance, *Small*, 2019, **15**, 1904240.

60 Y. C. Liang and C. W. Chang, Improvement of ethanol gas-sensing responses of ZnO-WO$_3$ composite nanorods through annealing induced local phase transformation, *Nanomaterials*, 2019, **9**, 669.

61 B. Yang, N. V. Myung and T. T. Tran, 1D metal oxide semiconductor materials for chemiresistive gas sensors: A Review, *Adv. Electron. Mater.*, 2021, 202100271.

62 P. Hao, P. Song, Z. Yang and Q. Wang, Synthesis of novel RuO$_2$/LaFeO$_3$ porous microspheres its gas sensing performances towards triethylamine, *J. Alloys Compd.*, 2019, **806**, 960–967.

63 C. Wang, S. Zhang, L. Qiu, S. A. Rasaki, F. Qu, T. Thomas, *et al.*, Ru-decorated WO$_3$ nanosheets for efficient xylene gas sensing application, *J. Alloys Compd.*, 2020, **826**, 154196.

64 L. Zhang, K. Doyle-Davis and X. Sun, Pt-based electrocatalysts with high atom utilization efficiency: from nanostructures to single atoms, *Energy Environ. Sci.*, 2019, **12**, 492–517.